Atmospheric
Measurement
Techniques
Discussions

A shape model of internally mixed soot particles derived from artificial surface tension

Hiroshi Ishimoto[1], Rei Kudo[1], Kouji Adachi[1]

[1]Meteorological Research Institute, Tsukuba, 305-0052, Japan

5   *Correspondence to*: Hiroshi Ishimoto (hiroishi@mri-jma.go.jp)

Abstract.

To retrieve the physical properties of aerosols from multi-channel ground-based/satellite measurements, we developed a shape model of coated soot particles and created a dataset of their optical properties. Bare soot particles were assumed to have an aggregate shape, and two types of aggregates with different size–shape dependences were modeled using a polyhedral Voronoi

10   structure. To simulate the detailed shape properties of mixtures of soot aggregates and adhered water-soluble substances, we propose a simple model of surface tension derived from the artificial surface potential. The light-scattering properties of the modeled particles with different volume fractions of water-soluble material were calculated using the finite-difference time-domain method and discrete-dipole approximation. The results of the single-scattering albedo and asymmetry factors were compared to those of conventional internally mixed spheres (i.e., effective medium spheres based on the Maxwell–Garnett

15   approximation and simple core–shell spheres). In addition, the lidar backscattering properties (i.e., lidar ratios and linear depolarization ratios) of the modeled soot particles were investigated. For internally mixed soot particles, the lidar backscattering properties were sensitive to the shape of the soot particles and the volume mixing ratio of the assumed water-soluble components. However, the average optical properties of biomass burning smoke, which have been reported from in situ field and laboratory measurements, were difficult to explain based on the individually modeled particle. Nonetheless, our

20   shape model and its calculated optical properties are expected to be useful as an alternative model for biomass burning smoke particles in advanced remote sensing via multi-channel radiometer and lidar measurements.

1 Introduction

During the atmosphere aging process of emitted combustion products, soot particles tend to become hydrophilic and form

25   mixtures with weakly light-absorbing materials (Adachi et al., 2007)(Shiraiwa et al., 2007) (Moteki and Kondo, 2007)(Mikhailov et al., 2006)(Adachi and Buseck, 2008) (Shiraiwa et al., 2010). Because of significant enhancements in light absorption and scattering, it has been suggested that soot particles in a mixing state are the second-most important contributor to global warming after carbon dioxide (Jacobson, 2001)(Ramanathan et al., 2008). For climate monitoring and numerical prediction via atmospheric data assimilation, precise estimation of the amount of mixed soot particles and the fraction of soot

Atmospheric
Measurement
Techniques
Discussions

(black carbon) from satellite-/ground-based remote-sensing measurements is important (Kahnert et al., 2013). Thus, understanding the optical properties of internally mixed soot particles is essential to improve the retrieval accuracy of atmospheric soot particles (Hara et al., 2018). The light-scattering properties of internally mixed particles depend strongly on the complex refractive index of each mixing component. Furthermore, the shape of the incorporated soot particles and overall

5   particle shape in the mixing state significantly alter some of the scattering properties. In particular, particle shape is important for the interpretation of lidar backscattering measurements. Many shape models have been proposed for internally mixed soot particles and their light-scattering properties using the discrete-dipole approximation (DDA) and T-Matrix methods (Adachi et al., 2010)(Scarnato et al., 2012)(Cheng et al., 2014)(Dong et al., 2015)(Liu et al., 2016)(Mishchenko et al., 2016)(Moteki, 2016)(Zhang et al., 2017)(Wu et al., 2016)(Wu et al., 2017)(Kahnert, 2017)(Luo et al., 2018). However, the relationship

10   between mixing state/morphology and light-scattering properties is not well defined.

As an alternative model for soot particles in a mixing state, we developed a new shape model of internally mixed particles. We assumed that bare soot particles with fractal-like shapes were mixed with water-soluble (WS) components. Moreover, we considered hydrophilic soot particles with high wettability due to atmospheric aging. The shapes of the mixed particles were determined by applying artificial potential calculations of the surface tension of the WS components. The numerical results of

15   the light-scattering properties of the modeled particles at visible and near-infrared wavelengths are discussed.

2 Shape model of internally mixed aerosols

2.1 Soot model

Bare soot particles are commonly described as fractal aggregates formed from primary particles (or monomers) with a degree

20   of overlapping and necking between neighboring primary particles (Yon et al., 2015)(Okyay et al., 2016). Primary particles have a diameter of 20–50 nm (Bond and Bergstrom, 2006) , and the fractal dimension of the aggregates depends on their emission condition and atmospheric aging. For example, newly generated soot aggregates often form lace-like structures with relatively small fractal dimensions, whereas aged soot aggregates tend to be compact and to be characterized by large fractal dimensions (Mikhailov et al., 2001)(Mikhailov et al., 2006)(Zhang et al., 2016). In this study, we modeled soot aggregates

25   using spatial Poisson–Voronoi tessellation. The basic methods to make the aggregate model are the same as those of dust particles and ice aggregates described in our previous works (Ishimoto et al., 2010)(Ishimoto et al., 2012a)(Ishimoto et al., 2012b) (Baran et al., 2018). A spatial Poisson–Voronoi tessellation was produced from randomly distributed nucleation points in the numerical field, and polyhedral cells overlapping with the assumed fractal frame were selected from the tessellation (Ishimoto et al., 2012a). We regarded the cells (i.e., Voronoi cells) as the primary soot aggregate particles to mimic overlapping

30   and necking between neighboring primary particles. To ensure that the size of the Voronoi cells was relatively uniform, we applied a Matérn hard-core point field (Ohser and Mücklich, 2000) to the spatial distribution of the nucleation points (Ishimoto et al., 2012b). The average volume of the Voronoi cells V_c in the tessellation is derived as

$$V_c = \frac{1}{\rho} = \frac{4}{3}\pi h^3, \qquad (1)$$

where ρ and h are the spatial density of the nucleation points and hard-core distance (i.e., minimum distance between the nucleation points), respectively. Aggregate particles of different sizes were produced in the same manner but by changing the relative size of the fractal frame in the same tessellation. Figure 1 shows two sets of aggregate particles (Type-A and Type-B)

5 created from fractal frames of different shapes. For the calculations of the light-scattering properties, 10 sizes of aggregates for Type-A and 13 sizes for Type-B (where No. 1, 2, and 3 were used for both sets) were prepared. A mean radius of the primary particle $a = 20$ nm was used as a typical value (Wu et al., 2017)(Wu et al., 2015)(Mishchenko et al., 2016)(Luo et al., 2018), and the total size of each aggregate was corrected by adjusting the average cell volume of the aggregate as $V_{c,\text{agg}} = 4/3\pi a^3$. Although the aggregates in Figure 1 were created using a box-counting approach to maintain a fractal relationship between size and shape, the fractal relationship differed from that of the commonly used fractal dimension D_f for describing

10 individual soot particles. The fractal dimension D_f is defined from the number of monomers N, fractal prefactor k_0, and gyration radius R_g as (Adachi et al., 2007)

$$N = k_0 \left(\frac{R_g}{a}\right)^{D_f}. \qquad (2)$$

For the numerical simulation of the light-scattering properties of aged soot particles, various D_f values with a typical prefactor

15 of $k_0 = 1.2$ have been proposed in the literature, such as $D_f = 2.0 - 2.5$ (Nyeki and Colbeck, 1995), $1.9 - 2.6$ (Adachi et al., 2007), 2.5 (He et al., 2015), 2.6 (Mishchenko et al., 2016), and $2.5 - 3.0$ (Zhang et al., 2017). The corresponding D_f values of our modeled soot particles derived from the calculation of R_g are plotted in Figure 2. Applying the fractal prefactor $k_0 = 1.2$ resulted in aggregate particles in the range of $D_f = 1.9 - 2.5$ (Type-A) and $2.5 - 3.0$ (Type-B) given a normalized gyration radius of $\ln(R_g/a) \leq 3.6$.
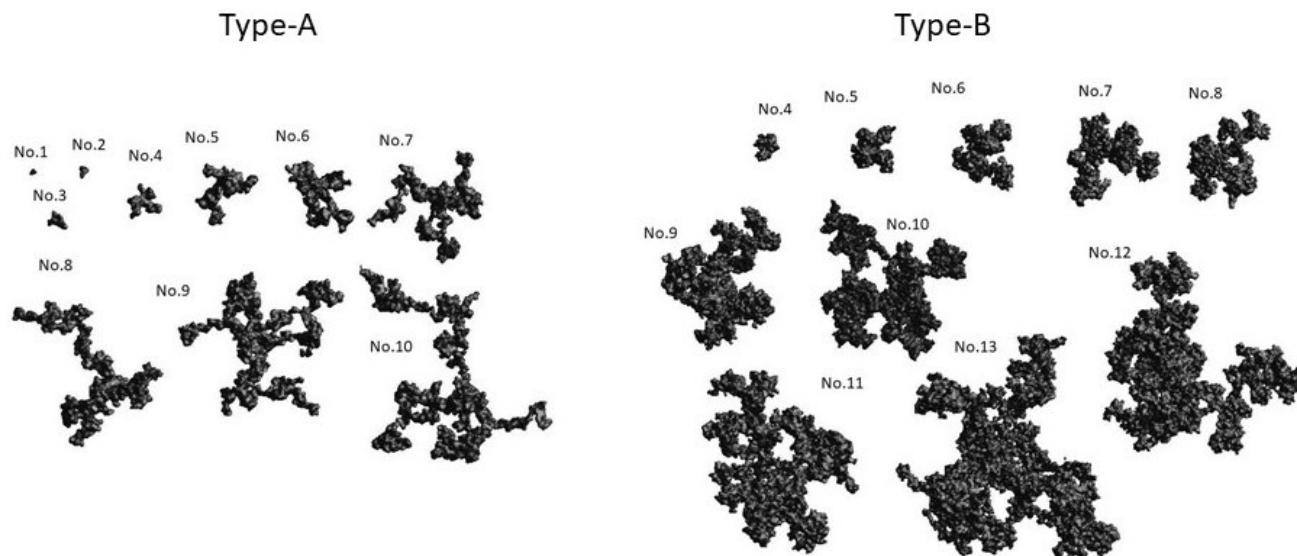
Figure 1: Model of bare soot particles created using three-dimensional Voronoi tessellation (Type-A and Type-B).
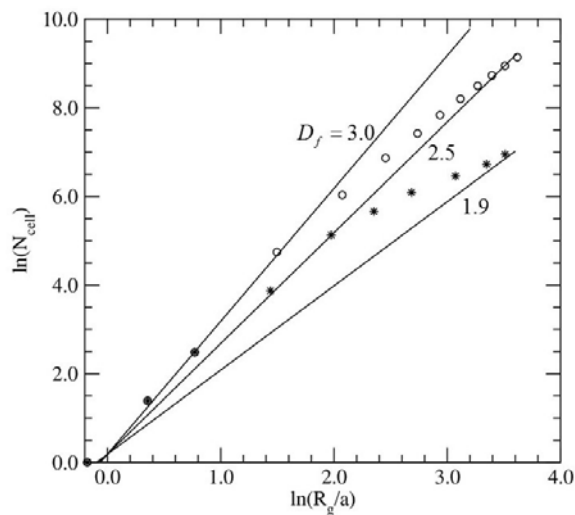
Figure 2: Relationship between the number of cells N_{cell} [assuming $N_{cell} = N$ from Eq. (2)] and normalized gyration radius R_g/a for the modelled soot aggregates. The asterisks and open circles correspond to Type-A and Type-B aggregates, respectively. The solid lines represent the relationship of Eq. (2) for fractal dimensions of $D_f = 1.9, 2.5, 3.0$ when $k_0 = 1.2$.

Atmospheric
Measurement
Techniques
Discussions

2.2 Artificial surface tension of mixed soot and water-soluble components

According to microscopic images of internally mixed soot particles, soot particles are often entirely encapsulated in a spherical shell and completely covered by WS components (Reid and Hobbs, 1998)(Reid et al., 2005a). This implies that WS components behave as a liquid on the particle surface; thus, the surface tension of WS components is important in describing the overall mixed particle shape. In this work, we examined a virtual potential field on the surface of the modeled particles to simulate a morphological effect by surface tension. We assumed that the dynamic behavior of liquid could be simulated by the movement of liquid elements from locations of high potential to locations of low potential. From a simple explanation of surface tension on a molecular scale, the potential at a surface point becomes smaller as the number of surrounding molecules increases. Therefore, the modeled particles were projected in a three-dimensional Cartesian grid space (grid length: l), and the artificial surface potential was defined as an analogue of the microscopic surface potential.

$$U_j \equiv -\sum_i f_i , \qquad \begin{cases} f_i = 1 & (r_i \leq d) \\ f_i = 0 & (r_i > d) \end{cases} \qquad (3)$$

where U_j is the artificial potential at surface point j, and U_j is defined as the negative value of the total number of grid points of material with a distance of r less than d. We used this simple model for the surface potential calculations to focus on the shape of the mixture in a discrete grid space. An equilibrium mixing state was simulated assuming that the applied WS components preferentially accumulate at grid points of lower potential. The shape of internally mixed particles under an arbitrary volume mixing ratio was determined based on iterative calculations of the surface potential and by adding WS elements. In the artificial potential calculations in Eq. (3), setting of the length d is important. We applied two steps for the potential calculations and adhesion of WS components for each iterative calculation.

$$d_1 = 3l , \qquad N_{add} = 0.016 N_s$$

$$d_2 = Max(d_1, d_{cor}) , \quad N_{add} = 0.004 N_s, \qquad (4)$$

where d_1 and d_2 are the lengths d for first and second steps, and N_{add} is the number of grid points for WS adhesion, which are chosen from the total surface points N_s (note that the surface point is defined as an empty grid and neighbor of an occupied grid). The value d_1 was determined from the results of preliminary calculations. Small d_1 values resulted in a coated particle with a thin layer at a local scale. By contrast, WS components tended to accumulate in the same region on particles when a large d_1 was applied. The second step in Eq. (4) is important, especially when WS components cover the entire soot aggregate, and the value d_2 is determined to ensure that the overall shape of the mixed particle is spherical. The correction length d_{cor} is the minimum length at which the curvature of the sphere with a radius R can be discriminated from the calculated artificial potential in the grid field, and d_{cor} is estimated from the following relationships.

$$\frac{4}{3}\pi R^3 = N_V l^3 , \quad 4\pi R^2 \gamma = N_s l^3, \quad R\sin\theta = d_{cor}, \quad R\cos\theta = R - l \qquad (5)$$

$$d_{cor} = l\sqrt{\frac{6N_V\gamma}{N_s l} - 1} \qquad (6)$$

where N_V is the total number of grid points occupied by the material, and γ is the effective skin depth ($\gamma = 1.51l$). Figure 3 presents a schematic diagram describing d_{cor} in a two-dimensional case.
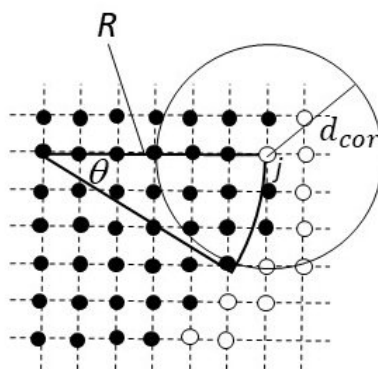

Figure 3: Schematic diagram of the distance d_{cor} based on the artificial potential calculation in a two-dimensional case. The open circles represent the surface points for the potential field calculation, and the solid circles indicate the points occupied by material. To discriminate the curvature of the radius R from the calculated potential at surface point j, the length d in Eq. (3) should be larger than d_{cor}. A spherical mixed particle is automatically generated from the potential calculations and the addition of water-soluble material when the soot particle is completely encapsulated.

The artificial potential was calculated for each iterative step, and N_{add} of WS elements was added starting with the grid points of lowest potential. The internally mixed soot model (i.e., the particle shape modeled based on artificial surface tension, AST hereafter) was created for different values of the volume ratio $V_r = V_{ws}/V_{soot}$, where V_{ws} and V_{soot} are the volumes of the WS and soot materials, respectively. Figure 4 shows the results of several mixed soot models for $V_r \sim 0, 2, 5, 10, 20$. For simplicity, we neglect the difference of materials (i.e., soot or WS) in the potential calculations of Eq. (3), which implicitly assumes that the soot material is sufficiently hydrophilic and has high WS wettability. Although we used assumptions to model these particles, their shapes are similar to those observed using an electron microscopy (Adachi et al., 2010; Fig. 5). The shape model of the particle was ultimately defined using a three-dimensional rendering technique.

Atmospheric
Measurement
Techniques
Discussions
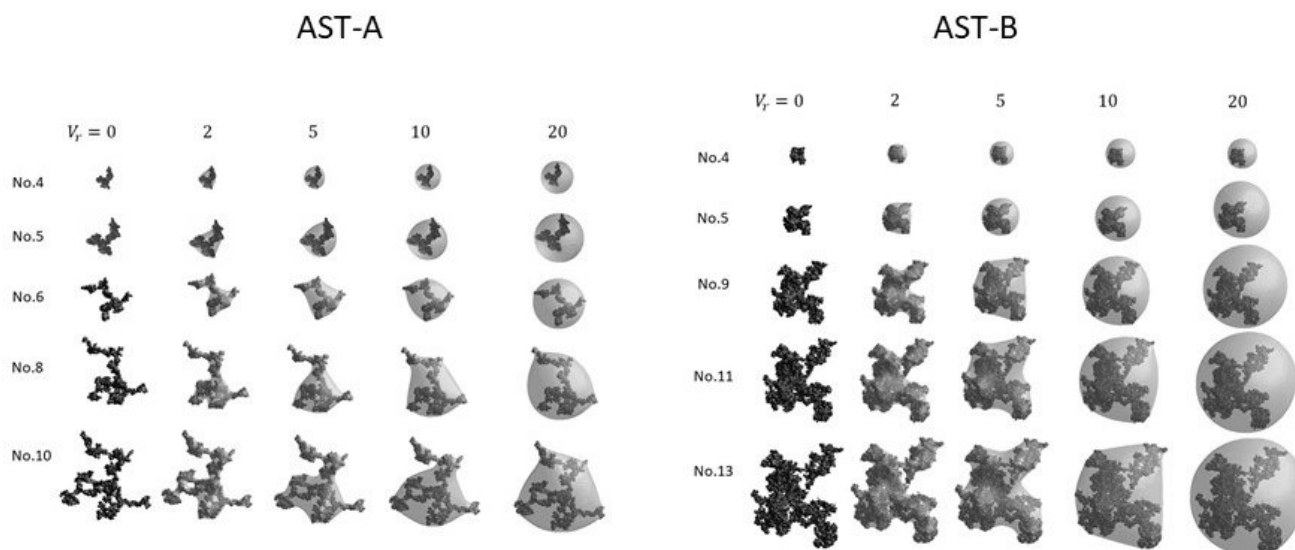
Figure 4: Mixed soot particle model developed using artificial surface tension (AST) for the attached water-soluble material. Several Type-A (Type-B) aggregates of different sizes were used on the left (right) side. The marching cubes method was applied for surface rendering.
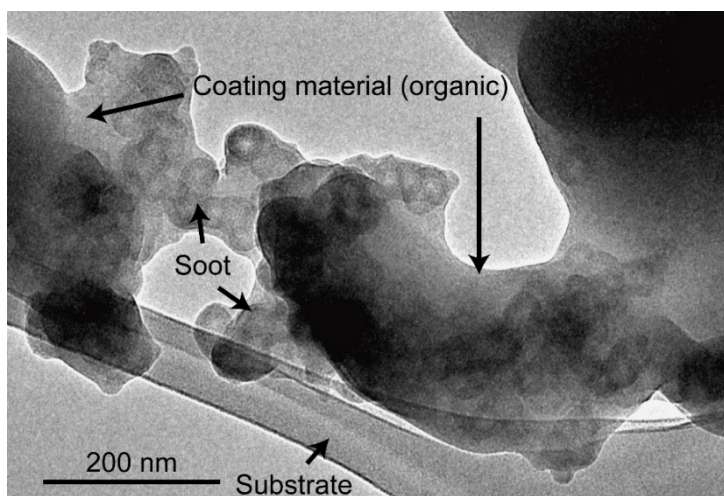
Figure 5: An example of transmission electron microscopy (TEM) image of internally mixed soot particle. The sample was collected from a biomass burning during the Biomass Burning Observation Project (BBOP) (Adachi et al., 2018). The soot particle has an aggregate structure of spherical monomers and is embedded within organic material. This particle looks similar to the AST-A particles (e.g., No.6 particle with $V_r = 5$ in Fig. 4).

3 Single-scattering properties

We calculated the light-scattering properties using the finite-difference time-domain (FDTD) method (Taflove and Hagness, 2005) (Cole, 2005) (Ishimoto et al., 2012a) and DDA [DDSCAT ver.7.3, http://www.ddscat.org/ (Draine and Flatau, 1994)]. Particles defined by discrete points as the input for the light-scattering calculations were reconstructed from the shape model described in Section 2, and the grid length was set within the range $2 \leq 2a/l \leq 10$ for a correct reproduction of the defined aggregates within the numerical convergence criterion. Although soot particles are generally small aerosols, large computational resources for FDTD and DDA calculations are necessary to estimate the exact scattering properties of the mixed particles due to the fine structure of soot and additional volume contributed by WS material. Using the same discretized particle under an appropriate convergence condition, the scattering properties calculated by FDTD would have approximately the same accuracy as those derived from DDA (Yurkin et al., 2007). However, the numerical cost of the two methods differs depending on the particle shape. The memory and CPU time of the DDA calculations mainly depend on the number of discretized points (i.e., dipoles) and are dependent on particle volume. Meanwhile, the numerical costs of the FDTD calculations are determined by the size of the discretized numerical field that encloses the particle. For fractal-shaped particles of relatively small fractal dimensions, DDA calculations are faster than FDTD ones because of the small relative volume with respect to size. By contrast, the numerical cost of DDA calculations drastically increases as the volume of attached WS elements increases, whereas the FDTD method can output results within similar CPU times given similar total sizes. Therefore, we used both numerical methods for the light-scattering calculations in accordance with the size and shape of the particles. As indicated in Section 2 and shown in Figures 1 and 2, 10 sizes of bare soot aggregates with a volume-equivalent sphere radius $r_{eq} = 0.02 - 0.20$ µm for Type-A and 13 sizes with $r_{eq} = 0.02 - 0.42$ µm for Type-B were prepared, and internally mixed particles of $V_r \sim 0, 2, 5, 10, 20$ were numerically created for each soot particle. The corresponding size ranges of the mixed soot particles were $r_{eq} = 0.02 - 0.55$ µm for Type-A (AST-A) and $r_{eq} = 0.02 - 1.15$ µm for Type-B (AST-B). Assuming a synthetic analysis using satellite-/ground-based multi-channel radiometer and lidar measurements, 10 wavelengths from near-ultraviolet to near-infrared (340, 355, 380, 400, 500, 532, 675, 870, 1020, 1064 nm) were selected. We used a spectral refractive index dataset by (Chang and Charalampopoulos, 1990) for the bare soot material. For the WS components, the dependence of the refractive index on relative humidity was considered, and relative humidity values of 0%, 50%, 90%, and 98% in the software package Optical Properties of Aerosols and Clouds (OPAC) were applied (Hess et al., 1998). The outputs included the results of the light-scattering properties with those averaged over 88 orientations for the FDTD method and 100 orientations for the DDA method.

As examples of the numerical results, Figures 5 and 6 present the size (r_{eq}) dependence of single-scattering albedo (ω) and the asymmetry factor (g) at wavelength of $\lambda = 532$ nm for AST-A. The complex refractive index $1.723 + 0.5837\,i$ for soot and $1.437 + 2.982 \times 10^{-3}\,i$ for WS components under a relative humidity 50%, were used. For comparison, the results of ω and g with the same V_r but derived via Mie calculations for spheres of the effective refractive index calculated using the Maxwell–Garnett mixing rule (MG) and for spheres with a soot-core/WS-shell structure (CS) were also plotted.

For ω and g at $\lambda = 532$ nm, the results of the AST model were approximately consistent with previous modeled results (Dong et al., 2015) (Liu et al., 2016). The results of ω for AST-A at $V_r = 0$ markedly differed from those of MG/CS because of the volume-equivalent sphere approximation in the MG/CS treatments. Meanwhile, the results of ω for AST-A with $V_r \geq 2$ showed a similar trend to the MG/CS results such that the MG results were closer to AST-A than CS was. Regarding the asymmetry factor, g depends mainly on the particle size r_{eq} and is less sensitive to the mixing ratio V_r. The derived g for AST-A fell between the results of MG and of CS in that the MG results were closer to those of AST-A. Because the primary particle of the assumed soot (a = 0.02 µm) was smaller than the wavelength and the Type-A aggregates were fractal shapes with relatively small D_f (Figs. 1 and 2), the effective medium theory based on the MG mixing rule offered a better approximation than did the CS approximation for the AST-A model.
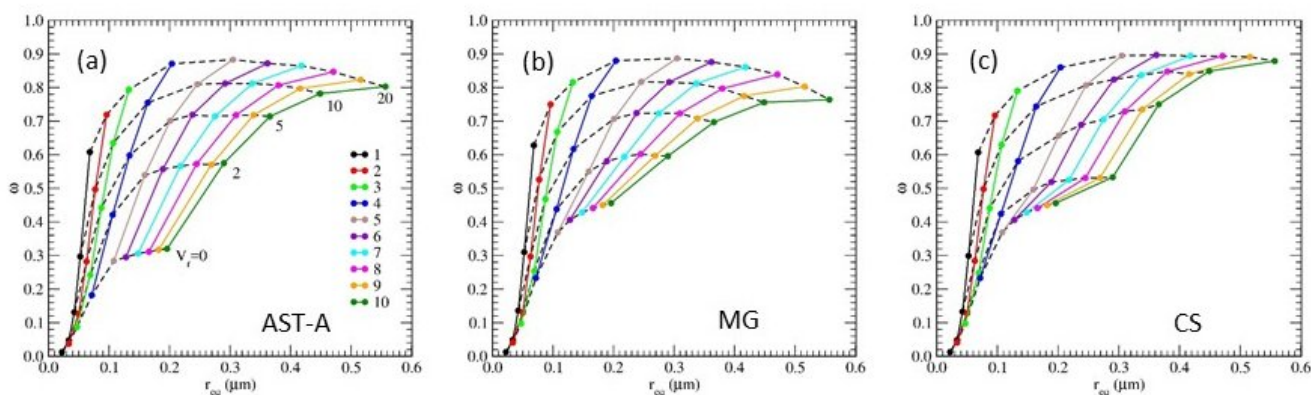
Figure 6: Single scattering albedo ω versus particle size (volume-equivalent sphere radius: r_{eq}) at wavelength of $\lambda = 532$ nm for the (a) AST model of Type-A aggregates (AST-A), (b) Maxwell-Garnett approximation (MG), and (c) core-shell approximation (CS). The results for the same bare soot aggregate at different volume ratios of $V_r \sim 0, 2, 5, 10, 20$ are plotted as the same color. The aggregate numbers are the same as those in Fig. 1.
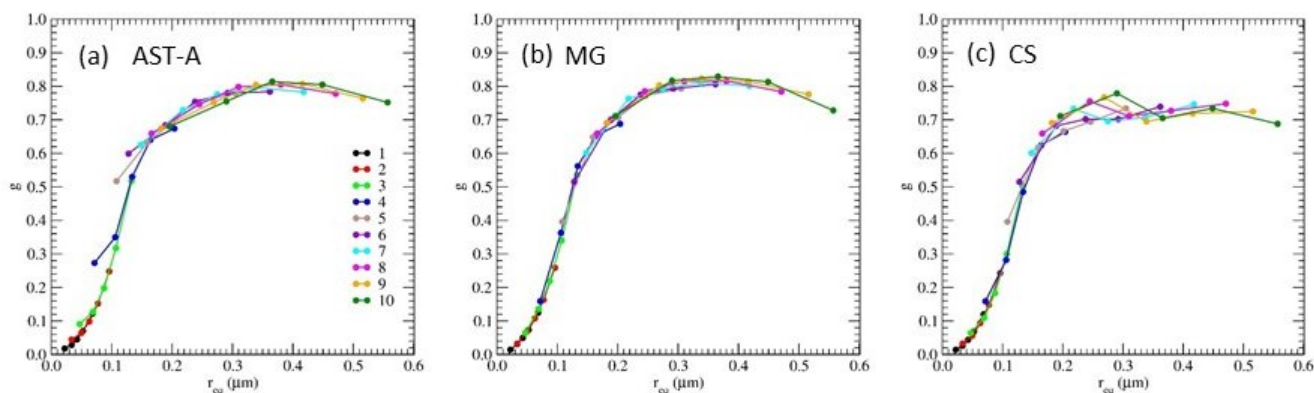

Figure 7: The same as Fig. 6, but the results for the asymmetry factor g.

Atmospheric
Measurement
Techniques
Discussions

Compared to ω and g, the backscattering properties of particles are sensitive to particle shape and mixing state. Therefore, lidar measurements could potentially offer information on the validity of the particle model. The calculated lidar ratio L and linear depolarization ratio δ_L for the AST-A particles at wavelengths of 355, 532, and 1064 nm are plotted in Figure 8. For a single particle, L is calculated from ω and the normalized phase function P_{11} in the backscattering direction, and δ_L is derived from the P_{11} and P_{22} components of the scattering matrix. Here, we omitted the backscattering of P_{12} for δ_L due to the assumption of particle random orientation.

$$L = \frac{4\pi}{\omega\, P_{11}}, \delta_L = \frac{P_{11} - P_{22}}{P_{11} + P_{22}} \qquad (7)$$

We applied the refractive indices for soot and WS components at a relative humidity of 50% at wavelengths of 355 and 1064 nm ($1.392 + 0.6985\, i$ and $1.441 + 2.649 \times 10^{-3}\, i$ at $\lambda = 355$ nm; $1.830 + 0.5573\, i$ and $1.427 + 8.691 \times 10^{-3}\, i$ at $\lambda = 1064$ nm). According to the results of measurements for biomass burning smoke events, the size of dry particles is $0.10 - 0.16$ μm at count median diameter ($0.25 - 0.30$ μm at volume median diameter) (Reid et al., 2005a). Meanwhile, laboratory and in situ measurements for aged biomass burning smoke have yielded estimations of $\omega \geq 0.75$ and $g \sim 0.6$ at $\lambda = 532$ nm (Reid et al., 2005b)(Pokhrel et al., 2016). For lidar measurements, typical values of $L \sim 70$ sr and $\delta_L \sim 7$ % at $\lambda = 532$ nm have been reported (Groß et al., 2015a)(Groß et al., 2015b). In our results of the optical properties for AST-A, particle No. 4 ($V_r = 20$) had values of $(\omega, g, L, \delta_L) = (0.87, 0.67, 69\text{ sr}, 0\text{ %})$, and particle No.5 ($V_r = 2$) had values of $(\omega, g, L, \delta_L) = (0.54, 0.63, 188\text{ sr}, 6\text{ %})$. Using the refractive index of a typical soot particle, relatively high values of V_r would be necessary to simulate $\omega \geq 0.75$. In the AST model, the soot aggregate was entirely encapsulated by WS components, and the overall shape became spherical under large V_r values. Although such spherical particles have consistent lidar ratios of $L \sim 70$ sr, the depolarization ratio becomes $\delta_L \sim 0$ for spherical shapes. By contrast, large depolarization ratios can be represented if the internally mixed particles are highly non-spherical. Moreover, the reported spectral dependence of depolarization ratios $(\delta_{L,355\text{nm}} \sim 20\text{ %},\ \delta_{L,532\text{nm}} \sim 9\text{ %}, \delta_{L,1064\text{nm}} \sim 2\text{ %})$ from airborne measurements for smoke plumes by (Burton et al., 2015)(Mishchenko et al., 2016) can be explained, for example, by the AST-A particle No.6 ($V_r = 5 - 10$). However, such non-spherical mixed particles tended to have relatively large lidar ratios of $L \geq 100$ sr at $\lambda = 355, 532$ nm in the AST-A model.

The results of the lidar ratios and linear depolarization ratios for internally mixed Type-B particles (AST-B) are plotted in Figure 9. AST-B particles were relatively larger than AST-A particles, and the variations in L and δ_L for AST-B were greater than those for AST-A. In addition to the results for AST-A, the lidar ratios decreased as the volume ratio V_r increased when $r_{eq} \geq 0.3$ μm owing to their lower absorbance and more spherical shape. Meanwhile, relatively high linear depolarization ratios at visible wavelengths were derived for AST-B ($\delta_L \sim 0.4$ at $\lambda = 532$ nm) comparing to AST-A for volume ratios of $V_r = 5 - 10$. Overall, the results of Figures 7 and 8 suggest that the effects of internal mixing on lidar backscattering are strongly related to changes in absorption/shape properties due to mixing and bare soot particle size. However, it was difficult to simulate the average smoke optical properties (ω, g, L, δ_L) and their spectral dependence solely using AST-A or AST-B particles. In

the field measurements, the observed optical properties are the average of the particle size distribution. Our results indicate that the existence of large mixed soot particles may enhance the bulk δ_L of smoke.

The typical values of V_r for mixed biomass burning smoke particles likely depend on the relative humidity, concentrations of WS components, and the size/shape of soot aggregates. Furthermore, mixing of different aerosol types, such as dust in biomass

5 burning (Groß et al., 2011)(Groß et al., 2013), may be important for the interpretation of the measured optical properties. Improved retrieval calculations based on realistic aerosol simulations that consider particle size/shape distribution and other types of aerosol contamination are expected using our AST model for internally mixed soot particles.
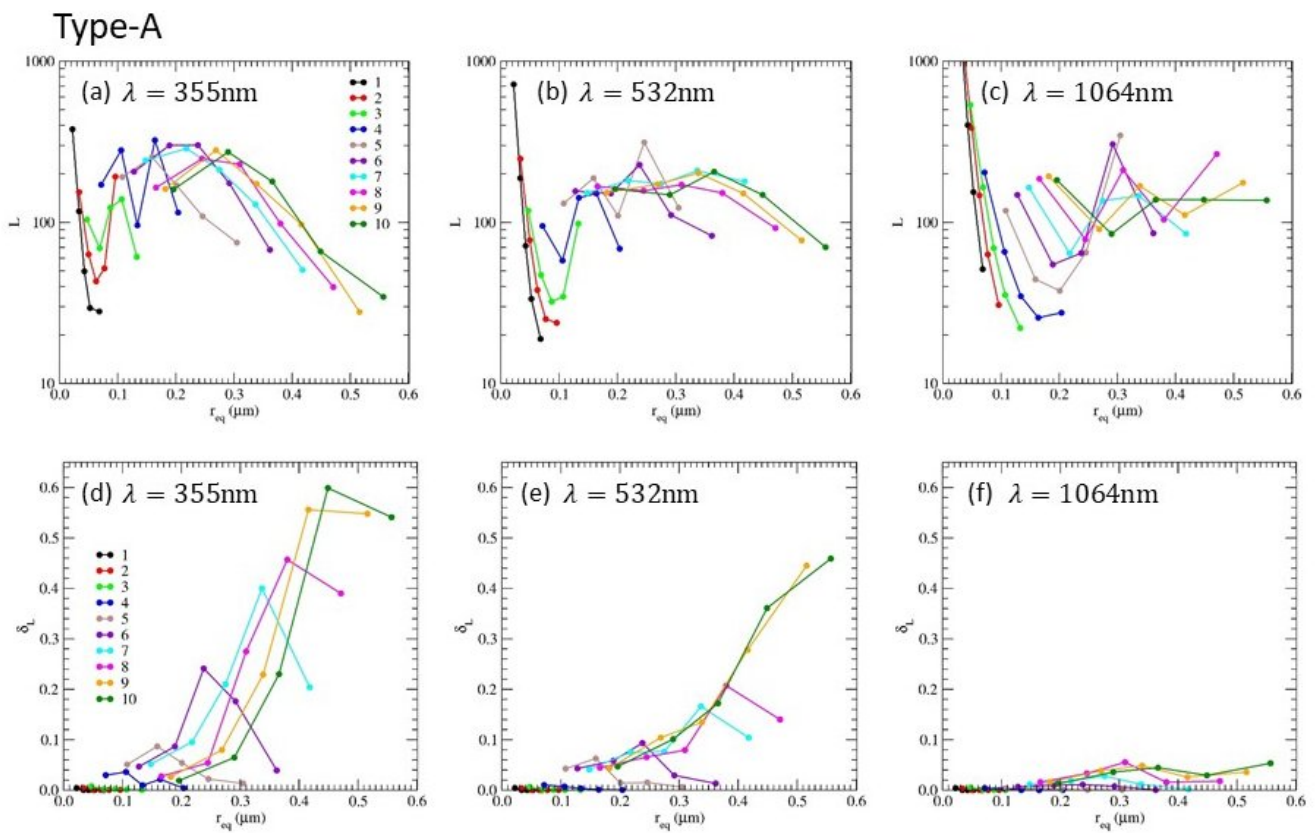
10

Figure 8: Results of the lidar ratio *L* for particles derived from AST-A model at wavelengths of (a) 355, (b) 532, and (c) 1064 nm. (d-f) The same as a-c but for the results of the linear depolarization ratio δ_L. The color and volume ratio V_r for each point of the calculation are the same as those in Fig. 6a ($V_r \sim 0, 2, 5, 10, 20$ from left to right for the same color of circles).
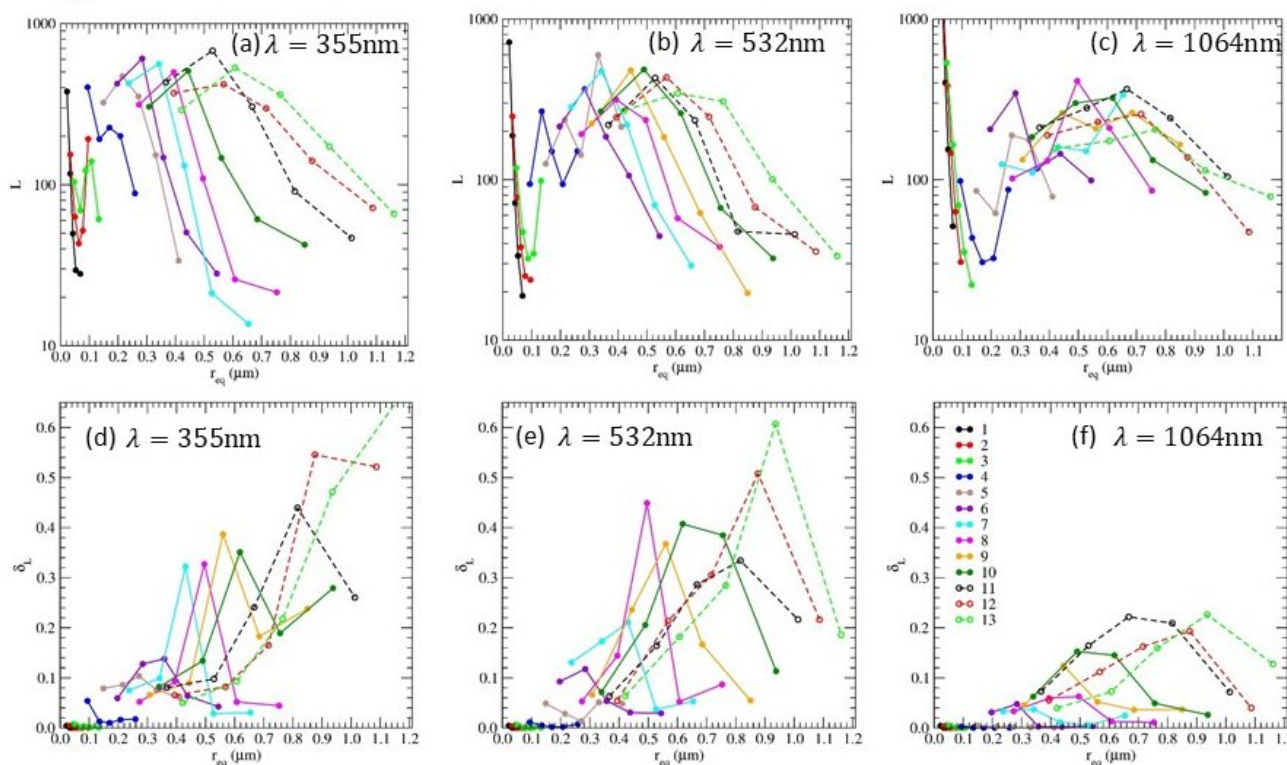
Atmospheric
Measurement
Techniques
Discussions

Figure 9: The same as Fig. 8, but for internally mixed Type-B particles (AST-B). Note that the horizontal scale differs from that in Fig. 8.

5

5 Summary

For satellite-/ground-based remote-sensing analysis applications, we developed a shape model of internally mixed soot particles and calculated the optical properties of particles at visible and near-infrared wavelengths. Fractal-like structures extracted using spatial Voronoi tessellation were considered to mimic necking and overlapping between neighboring primary

10 particles. We created two types of polyhedral aggregates with different particle shape–size dependences (Type-A and -B) to account for the effect of compaction on soot aggregate shape during the atmospheric aging process. Then, the artificial surface potential for the particle in a Cartesian grid space was defined, and the surface tension of the WS components on the soot aggregate was simulated, assuming that the soot was hydrophilic with high wettability. Based on a simple assumption of the behavior of WS elements, the shapes of internally mixed soot particles dependent on the amount of attached dissolved material

15 were determined from iterative calculations. Overall, an aggregate coated with a thin film was simulated given a relatively

Atmospheric
Measurement
Techniques
Discussions

small volume of added WS components, whereas the soot aggregate was covered with a spherical shell given a large amount of WS components. The optical properties of the developed internally mixed particles were calculated using the FDTD and DDA methods while considering the spectral dependence on the refractive indices. In addition to its use in direct analysis for the field measurement results, the dataset of the optical properties can be used for the parameterization of conventional
5   spherical particle models, such as the MG model, CS model, and their combined model. Furthermore, the dataset will be useful for determining the shape property conditions of smoke particles observed from multi-sensor measurements, including lidar backscattering.

Acknowledgements

References

Adachi, K. and Buseck, P. R.: Internally mixed soot, sulfates, and organic matter in aerosol particles from Mexico City,
15   Atmos. Chem. Phys., 8(21), 6469–6481, doi:10.5194/acp-8-6469-2008, 2008.

Adachi, K., Chung, S. H., Friedrich, H. and Buseck, P. R.: Fractal parameters of individual soot particles determined using electron tomography: Implications for optical properties, J. Geophys. Res. Atmos., 112(14), 1–10, doi:10.1029/2006JD008296, 2007.

Adachi, K., Chung, S. H. and Buseck, P. R.: Shapes of soot aerosol particles and implications for their effects on climate, J.
20   Geophys. Res. Atmos., 115(15), 1–9, doi:10.1029/2009JD012868, 2010.

Adachi, K., Sedlacek III, A. J., Kleinman, L., Chand, D., Hubbe, J. M. and Buseck, P. R.: Volume changes upon heating of aerosol particles from biomass burning using transmission electron microscopy, , c, doi:10.1080/02786826.2017.1373181, 2018.

Baran, A. J., Ishimoto, H., Sourdeval, O., Hesse, E. and Harlow, C.: The applicability of physical optics in the millimetre and
25   sub-millimetre spectral region. Part II: Application to a three-component model of ice cloud and its evaluation against the bulk single-scattering properties of various other aggregate models, J. Quant. Spectrosc. Radiat. Transf., 206, 83–100, doi:10.1016/j.jqsrt.2017.10.027, 2018.

Bond, T. C. and Bergstrom, R. W.: Light absorption by carbonaceous particles: An investigative review, Aerosol Sci. Technol., 40(1), 27–67, doi:10.1080/02786820500421521, 2006.

Burton, S. P., Hair, J. W., Kahnert, M., Ferrare, R. A., Hostetler, C. A., Cook, A. L., Harper, D. B., Berkoff, T. A., Seaman, S. T., Collins, J. E., Fenn, M. A. and Rogers, R. R.: Observations of the spectral dependence of linear particle depolarization ratio of aerosols using NASA Langley airborne High Spectral Resolution Lidar, Atmos. Chem. Phys., 15(23), 13453–13473, doi:10.5194/acp-15-13453-2015, 2015.

5   Chang, H. and Charalampopoulos, T. T.: Determination of the Wavelength Dependence of Refractive Indices of Flame Soot, Proc. R. Soc. A Math. Phys. Eng. Sci., 430(1880), 577–591, doi:10.1098/rspa.1990.0107, 1990.

Cheng, T., Gu, X., Wu, Y. and Chen, H.: Effects of atmospheric water on the optical properties of soot aerosols with different mixing states, J. Quant. Spectrosc. Radiat. Transf., 147, 196–206, doi:10.1016/j.jqsrt.2014.06.002, 2014.

Cole, J. B.: High accuracy nonstandard finite-difference time-domain algorithms for computational electromagnetics:

10   Applications to optics and photonics, in Advances in the Applications of Nonstandard Finite Difference Schemes, edited by R. E. Mickens, pp. 89–189, World Scientific., 2005.

Dong, J., Zhao, J. M. and Liu, L. H.: Morphological effects on the radiative properties of soot aerosols in different internally mixing states with sulfate, J. Quant. Spectrosc. Radiat. Transf., 165, 43–55, doi:10.1016/j.jqsrt.2015.06.025, 2015.

Draine, B. T. and Flatau, P. J.: Discrete-Dipole Approximation For Scattering Calculations, J. Opt. Soc. Am. A, 11(4), 1491,

15   doi:10.1364/JOSAA.11.001491, 1994.

Groß, S., Tesche, M., Freudenthaler, V., Toledano, C., Wiegner, M., Ansmann, A., Althausen, D. and Seefeldner, M.: Characterization of Saharan dust, marine aerosols and mixtures of biomass-burning aerosols and dust by means of multi-wavelength depolarization and Raman lidar measurements during SAMUM 2, Tellus, Ser. B Chem. Phys. Meteorol., 63(4), 706–724, doi:10.1111/j.1600-0889.2011.00556.x, 2011.

20   Groß, S., Esselborn, M., Weinzierl, B., Wirth, M., Fix, A. and Petzold, A.: Aerosol classification by airborne high spectral resolution lidar observations, Atmos. Chem. Phys., 13(5), 2487–2505, doi:10.5194/acp-13-2487-2013, 2013.

Groß, S., Freudenthaler, V., Schepanski, K., Toledano, C., Schäfler, A., Ansmann, A. and Weinzierl, B.: Optical properties of long-range transported Saharan dust over Barbados as measured by dual-wavelength depolarization Raman lidar measurements, Atmos. Chem. Phys., 15(19), 11067–11080, doi:10.5194/acp-15-11067-2015, 2015a.

25   Groß, S., Freudenthaler, V., Wirth, M. and Weinzierl, B.: Towards an aerosol classification scheme for future EarthCARE lidar observations and implications for research needs, Atmos. Sci. Lett., 16(1), 77–82, doi:10.1002/asl2.524, 2015b.

Hara, Y., Nishizawa, T., Sugimoto, N., Osada, K., Yumimoto, K., Uno, I., Kudo, R. and Ishimoto, H.: Retrieval of Aerosol Components Using Multi-Wavelength Mie-Raman Lidar and Comparison with Ground Aerosol Sampling, Remote Sens., 10(6), 937, doi:10.3390/rs10060937, 2018.

30   He, C., Liou, K. N., Takano, Y., Zhang, R., Levy Zamora, M., Yang, P., Li, Q. and Leung, L. R.: Variation of the radiative properties during black carbon aging: Theoretical and experimental intercomparison, Atmos. Chem. Phys., 15(20), 11967–11980, doi:10.5194/acp-15-11967-2015, 2015.

Hess, M., Koepke, P. and Schult, I.: Optical Properties of Aerosols and Clouds: The Software Package OPAC, Bull. Am. Meteorol. Soc., 79(5), 831–844, doi:10.1175/1520-0477(1998)079<0831:OPOAAC>2.0.CO;2, 1998.

Ishimoto, H., Zaizen, Y., Uchiyama, A., Masuda, K. and Mano, Y.: Shape modeling of mineral dust particles for light-scattering calculations using the spatial Poisson-Voronoi tessellation, J. Quant. Spectrosc. Radiat. Transf., 111(16), 2434–2443, doi:10.1016/j.jqsrt.2010.06.018, 2010.

Ishimoto, H., Masuda, K., Mano, Y., Orikasa, N. and Uchiyama, A.: Irregularly shaped ice aggregates in optical modeling of convectively generated ice clouds, J. Quant. Spectrosc. Radiat. Transf., 113(8), 632–643, doi:10.1016/j.jqsrt.2012.01.017, 2012a.

Ishimoto, H., Zaizen, Y., Masuda, K., Mano, Y. and Uchiyama, A.: Shape modeling of dust and soot particles for remote sensing applications considering the geometrical features of sampled aerosols, in Technical Reports of the Meteorological Research Institute, pp. 40–43. [online] Available from: http://www.mri-jma.go.jp/Publish/Technical/index_en.html, 2012b.

Jacobson, M. Z.: Strong radiative heating due to the mixing state of black carbon in atmospheric aerosols, Nature, 409(6821), 695–697, doi:10.1038/35055518, 2001.

Kahnert, M.: Optical properties of black carbon aerosols encapsulated in a shell of sulfate: comparison of the closed cell model with a coated aggregate model, Opt. Express, 25(20), 24579, doi:10.1364/OE.25.024579, 2017.

Kahnert, M., Nousiainen, T. and Lindqvist, H.: Models for integrated and differential scattering optical properties of encapsulated light absorbing carbon aggregates, Opt. Express, 21(7), 7974–7993, 2013.

Liu, F., Yon, J. and Bescond, A.: On the radiative properties of soot aggregates - Part 2: Effects of coating, J. Quant. Spectrosc. Radiat. Transf., 172, 134–145, doi:10.1016/j.jqsrt.2015.08.005, 2016.

Luo, J., Zhang, Y. and Zhang, Q.: A model study of aggregates composed of spherical soot monomers with an acentric carbon shell, J. Quant. Spectrosc. Radiat. Transf., 205, 184–195, doi:10.1016/j.jqsrt.2017.10.024, 2018.

Mikhailov, E. F., Vlasenko, S. S., Krämer, L. and Niessner, R.: Interaction of soot aerosol particles with water droplets: Influence of surface hydrophilicity, J. Aerosol Sci., 32(6), 697–711, doi:10.1016/S0021-8502(00)00101-4, 2001.

Mikhailov, E. F., Vlasenko, S. S., Podgorny, I. A., Ramanathan, V. and Corrigan, C. E.: Optical properties of soot-water drop agglomerates: An experimental study, J. Geophys. Res. Atmos., 111(7), doi:10.1029/2005JD006389, 2006.

Mishchenko, M. I., Dlugach, J. M. and Liu, L.: Linear depolarization of lidar returns by aged smoke particles, Appl. Opt., 55(35), 9968–9973, doi:10.1364/AO.55.009968, 2016.

Moteki, N.: Discrete dipole approximation for black carbon-containing aerosols in arbitrary mixing state: A hybrid discretization scheme, J. Quant. Spectrosc. Radiat. Transf., 178, 306–314, doi:10.1016/j.jqsrt.2016.01.025, 2016.

Nyeki, S. and Colbeck, I.: Fractal Dimension Analysis of Single, In-Situ, Restructured Carbonaceous Aggregates, Aerosol Sci. Technol., 23(2), 109–120, doi:10.1080/02786829508965298, 1995.

Ohser, J. and Mücklich, F.: Statistical Analysis of Microstructures in Materials Science, John Wiley & Sons., 2000.

Okyay, G., Héripré, E., Reiss, T., Haghi-Ashtiani, P., Auger, T. and Enguehard, F.: Soot aggregate complex morphology: 3D geometry reconstruction by SEM tomography applied on soot issued from propane combustion, J. Aerosol Sci., 93, 63–79, doi:10.1016/j.jaerosci.2015.11.009, 2016.

Pokhrel, R. P., Wagner, N. L., Langridge, J. M., Lack, D. A., Jayarathne, T., Stone, E. A., Stockwell, C. E., Yokelson, R. J. and Murphy, S. M.: Parameterization of single-scattering albedo (SSA) and absorption Ångström exponent (AAE) with EC/OC for aerosol emissions from biomass burning, Atmos. Chem. Phys., 16(15), 9549–9561, doi:10.5194/acp-16-9549-2016, 2016.

5 Ramanathan, V., Carmichael, G., V. Ramanathan and G. Carmichael, Ramanathan, V. and Carmichael, G.: Global and regional climate changes due to black carbon, Nat. Geosci., 1(4), 221–227, doi:10.1038/ngeo156, 2008.

Reid, J. S., Koppmann, R., Eck, T. F. and Eleuterio, D. P.: A review of biomass burning emissions, part II: Intensive physical properties of biomass burning particles, Atmos. Chem. Phys., 5, 799–825, doi:10.5194/acpd-4-5135-2004, 2005a.

Reid, J. S., Eck, T. F., Christopher, S. A., Koppmann, R., Dubovik, O., Eleuterio, D. P., Holben, B. N., Reid, E. A. and

10 Zhang, J.: A review of biomass burning emissions part III: intensive optical properties of biomass burning particles, Atmos. Chem. Phys., 5, 827–849, doi:10.5194/acpd-4-5201-2004, 2005b.

Reid, S. and Hobbs, P. V: Physical and optical properties of young smoke from individual biomass fires in Brazil, J. Geophys. Res., 103(D24), 32013–32030, 1998.

Scarnato, B., Vahidinia, S., Richard, D. T. and Kirchstetter, T. W.: Effects of internal mixing and aggregate morphology on

15 optical properties of black carbon using a discrete dipole approximation model, Atmos. Chem. Phys. Discuss., 12(10), 26401–26434, doi:10.5194/acpd-12-26401-2012, 2012.

Shiraiwa, M., Kondo, Y., Moteki, N., Takegawa, N., Miyazaki, Y. and Blake, D. R.: Evolution of mixing state of black carbon in polluted air from Tokyo, Geophys. Res. Lett., 34(16), 2–6, doi:10.1029/2007GL029819, 2007.

Shiraiwa, M., Kondo, Y., Iwamoto, T. and Kita, K.: Amplification of light absorption of black carbon by organic coating,

20 Aerosol Sci. Technol., 44(1), 46–54, doi:10.1080/02786820903357686, 2010.

Taflove, A. and Hagness, S. C.: Computational electrodynamics The finite-difference time-domain method, 3rd ed., Artech House., 2005.

Wu, Y., Cheng, T., Zheng, L., Chen, H. and Xu, H.: Single scattering properties of semi-embedded soot morphologies with intersecting and non-intersecting surfaces of absorbing spheres and non-absorbing host, J. Quant. Spectrosc. Radiat. Transf.,

25 157, 1–13, doi:10.1016/j.jqsrt.2015.02.006, 2015.

Wu, Y., Cheng, T., Zheng, L. and Chen, H.: Optical properties of the semi-external mixture composed of sulfate particle and different quantities of soot aggregates, J. Quant. Spectrosc. Radiat. Transf., 179, 139–148, doi:10.1016/j.jqsrt.2016.03.012, 2016.

Wu, Y., Cheng, T., Zheng, L. and Chen, H.: Sensitivity of mixing states on optical properties of fresh secondary organic

30 carbon aerosols, J. Quant. Spectrosc. Radiat. Transf., 195, 147–155, doi:10.1016/j.jqsrt.2017.01.013, 2017.

Yon, J., Bescond, A. and Liu, F.: On the radiative properties of soot aggregates part 1: Necking and overlapping, J. Quant. Spectrosc. Radiat. Transf., 162, 197–206, doi:10.1016/j.jqsrt.2015.03.027, 2015.

Yurkin, M. A., Hoekstra, A. G., Brock, R. S. and Lu, J. Q.: Systematic comparison of the discrete dipole approximation and the finite difference time domain method for large dielectric scatterers, Opt. Express, 15(26), 17902–17911, 2007.

Zhang, X., Mao, M., Yin, Y. and Wang, B.: Absorption enhancement of aged black carbon aerosols affected by their microphysics: A numerical investigation, J. Quant. Spectrosc. Radiat. Transf., 202, 90–97, doi:10.1016/j.jqsrt.2017.07.025, 2017.

Zhang, Y., Zhang, Q., Cheng, Y., Su, H., Kecorius, S., Wang, Z., Wu, Z., Hu, M., Zhu, T., Wiedensohler, A. and He, K.:

5   Measuring the morphology and density of internally mixed black carbon with SP2 and VTDMA: New insight into the absorption enhancement of black carbon in the atmosphere, Atmos. Meas. Tech., 9(4), 1833–1843, doi:10.5194/amt-9-1833-2016, 2016.